communications chemistry

ARTICLE

https://doi.org/10.1038/s42004-023-00907-4 OPEN

Impact of the metal core on the electrochemiluminescence of a pair of atomically precise Au_{20} nanocluster isomers

Shuang Chen[1,2,3,4,7✉], Ying Liu[1,2,3,4,7], Kaiyang Kuang[1,2,3,4,7], Bing Yin[1,2,3,4], Xiaojian Wang[1,2,3,4], Lirong Jiang[1,2,3,4], Pu Wang[5,6✉], Yong Pei[5,6✉] & Manzhou Zhu[1,2,3,4✉]

Although the electrochemiluminescence (ECL) of metal nanoclusters has been reported, revealing the correlation between structure and ECL at an atomic level is highly challenging. Here, we reported the impact of the metal core of $Au_{20}(SAdm)_{12}(CHT)_4$ (Au_{20}-AC for short; SAdm = 1-adamantanethiolate; CHT= cyclohexanethiol) and its isomer $Au_{20}(TBBT)_{16}$ (TBBT = 4-tert-butylthiophenol) on their solution-state and solid-state electrochemiluminescence. In self-annihilation ECL experiments, Au_{20}-AC showed a strong cathodic ECL but a weak anodic ECL, while the ECL signal of $Au_{20}(TBBT)_{16}$ was weak and barely detectable. Density functional theory (DFT) calculations showed that the Au_7 kernel of $[Au_{20}\text{-AC}]^-$ is metastable, weakening its anodic ECL. Au_{20}-AC in solution-state displayed an intense co-reactant ECL in the near-infrared region, which is 7 times higher than that of standard $Ru(bpy)_3^{2+}$. The strongest solid-state ECL emissions of Au_{20}-AC and $Au_{20}(TBBT)_{16}$ were at 860 and 770 nm, respectively — 15 nm red-shifted for Au_{20}-AC and 20 nm blue-shifted for $Au_{20}(TBBT)_{16}$, compared to their corresponding solid-state photoluminescence (PL) emissions. This work shows that ECL is significantly affected by the subtle differences of the metal core, and offers a potential basis for sensing and immunoassay platforms based on atomically precise emissive metal nanoclusters.

[1] Institutes of Physical Science and Information Technology, Anhui University, Hefei, Anhui 230601, PR China. [2] Centre for Atomic Engineering of Advanced Materials, Anhui University, Hefei, Anhui 230601, PR China. [3] Key Laboratory of Structure and Functional Regulation of Hybrid Materials of Ministry of Education, Anhui University, Hefei, Anhui 230601, PR China. [4] Department of Chemistry and Anhui Province Key Laboratory of Chemistry for Inorganic/Organic Hybrid Functionalized Materials, Anhui University, Hefei, Anhui 230601, PR China. [5] Department of Chemistry, Xiangtan University, Xiangtan, Hunan 411105, PR China. [6] Key Laboratory of Environmentally Friendly Chemistry and Applications of Ministry of Education, Xiangtan University, Xiangtan, Hunan 411105, PR China. [7] These authors contributed equally: Shuang Chen, Ying Liu, Kaiyang Kuang. ✉email: chenshuang@ahu.edu.cn; 90wangpu@xtu.edu.cn; ypnku78@gmail.com; zmz@ahu.edu.cn

Electrogenerated chemiluminescence entails the generation of electronically excited species at electrode surfaces which emit light upon their relaxation to a lower-level state. ECL is a highly sensitive and selective analytical technique, with a low detection limit in absence of background light[1–9]. Metal nanoclusters have been demonstrated to be excellent ECL luminophores due to their high intensity and efficiency[10–18]. Determined structure and fascinating properties of metal nanoclusters provide important insights for structure-property correlations and important guidance for designing functional nanomaterials[19–22]. Although progress of ECL of metal nanocluster has been made, the influence factors of ECL of metal nanoclusters have been unrevealed. Structural isomers of metal nanocluster are ideal models for understanding the effect of different structural moieties on ECL properties[23–26]. Thus far, only once case of correlation between structure and ECL property of metal nanocluster has been reported[27], yet whether the different influencing factors affect the behavior of ECLs in solution is still unknown. Recently, solid-state ECL (SSECL) has been developed after the aggregation-induced ECL (AIECL) proposed[28–33]. Aggregation-induced emission (AIE) materials provide the possibility for AIECL. In metal nanocluster, Xie et al. revealed gold nanoclusters with long Au-SR motifs could generate strong emissions due to the aggregation of motifs on the metal cores[32], which is desirable for the ECL of metal nanocluster in solid state.

Herein, we report the preparation and structure of $Au_{20}(SAdm)_{12}(CHT)_4$ (abbrev. Au_{20}-AC below, SAdm = 1-adamantanethiol, CHT = cyclohexanethiol), whose structure is similar to that of Au_{20}-Iso1, as predicted by Pei and co-workers[34]; Au_{20}-AC contain one Au_7 core, two $Au_2(SR)_3$, one $Au_3(SR)_4$ and one long $Au_6(SR)_6$ motif. We explored self-annihilation and coreactant ECLs of Au_{20}-AC and its isomer $Au_{20}(TBBT)_{16}$ (TBBT = 4-tert-butylthiophenol, reported by Jin et al.[35]) in solution and solid states. Electrochemistry, ECL, PL and density functional theory (DFT) simulation have been employed to establish a correlation between structure and ECL performance in different states. It is observed that Au_{20}-AC displayed an intense cathodic ECL and a weak anodic ECL, while $Au_{20}(TBBT)_{16}$ showed weak cathodic and anodic ECLs in self-annihilation pathway. DFT calculations indicate that the anion radical is destabilized due to metal core distortion for Au_{20}-AC, leading to weak anodic ECL. ECL spectrum of Au_{20}-AC in solution state is centered at 830 nm in the presence of TPrA. The oxidative reduction SSECL of both Au_{20} clusters in phosphate buffer solution (PBS, pH = 7.5) was observed in the near-infrared region. Overall, our correlation of the structure of these Au metal nanocluster isomers with their ECL performance constitutes a possible approach towards the design of intense ECL emitters and the development of associated detection platforms[6,36–38].

Results and discussion

Structure and characterization of Au_{20}-AC. Au_{20}-AC was formed by ligand etching $Au_{18}(CHT)_{14}$ nanoclusters with HSAdm[39] and purified by TLC. As shown in Supplementary Fig. 1, three bands corresponding to Au_{20}-AC, Au_{16} and Au_{21} nanoclusters from top to bottom, were observed. The UV-vis absorption spectra of these three nanoclusters are shown in Supplementary Fig. 2. Rhombic crystals of Au_{20}-AC could be obtained within 2~3 days using a mixture of methanol and CH_2Cl_2.

The structure of Au_{20}-AC was determined by single-crystal X-ray diffraction (Supplementary Data 1), which revealed that its crystals adopt the monoclinic space group C2/c. Full details are presented in Fig. 1 and Supplementary Table 1. Structurally, Au_{20}-AC is almost identical to the predicted Au_{20}-Iso1, and contains a

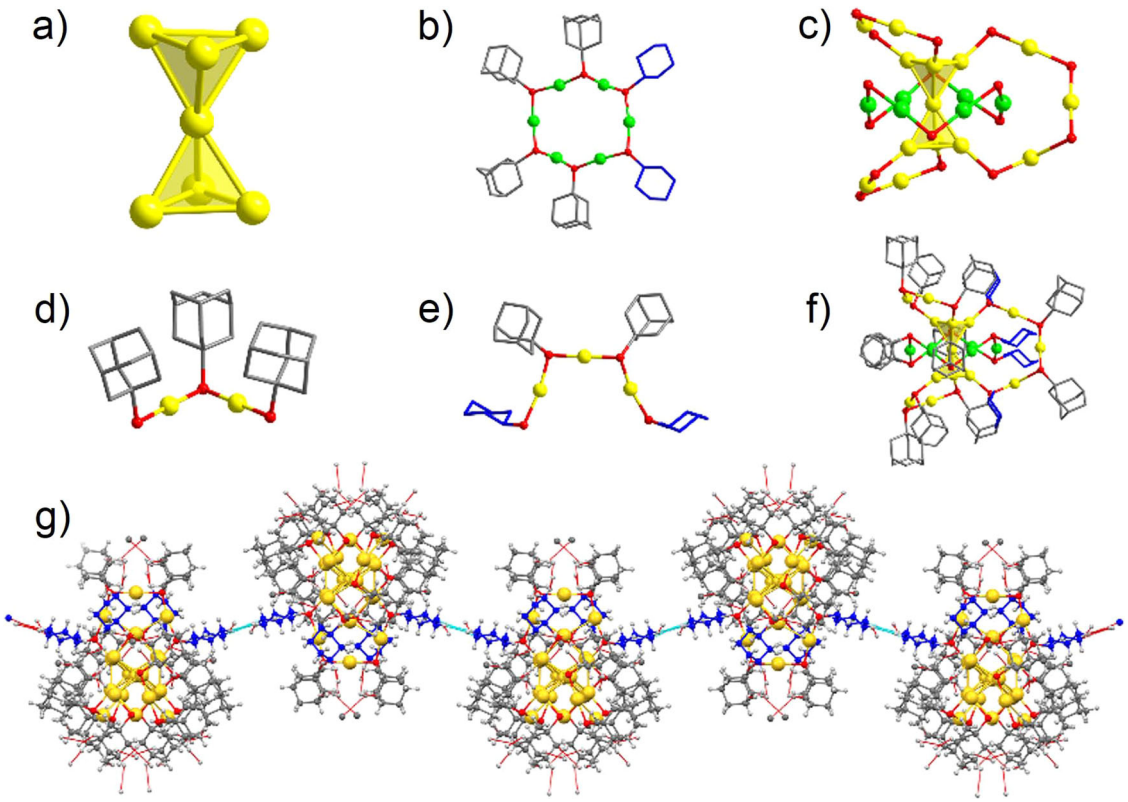

Fig. 1 Total structure of Au_{20}-AC. a The di-tetrahedral Au_7 kernel. **b** The circular $Au_6(SAdm)_4(CHT)_2$ motif. **c** The structure of kernel and motifs in $Au_{20}(SAdm)_{12}(CHT)_4$. **d** The dimeric $Au_2(SAdm)_3$ motif. **e** The trimeric $Au_3(SAdm)_2(CHT)_2$ motif. **f** The total structure of $Au_{20}(SAdm)_{12}(CHT)_4$, all H atoms are omitted for clarity. **g** The arrangement of cyclohexane rings in a head-to-head pattern in neighboring CHT of Au_{20}-AC. (Color labels: green, yellow = Au; red = S; grey, blue = C; white = H).

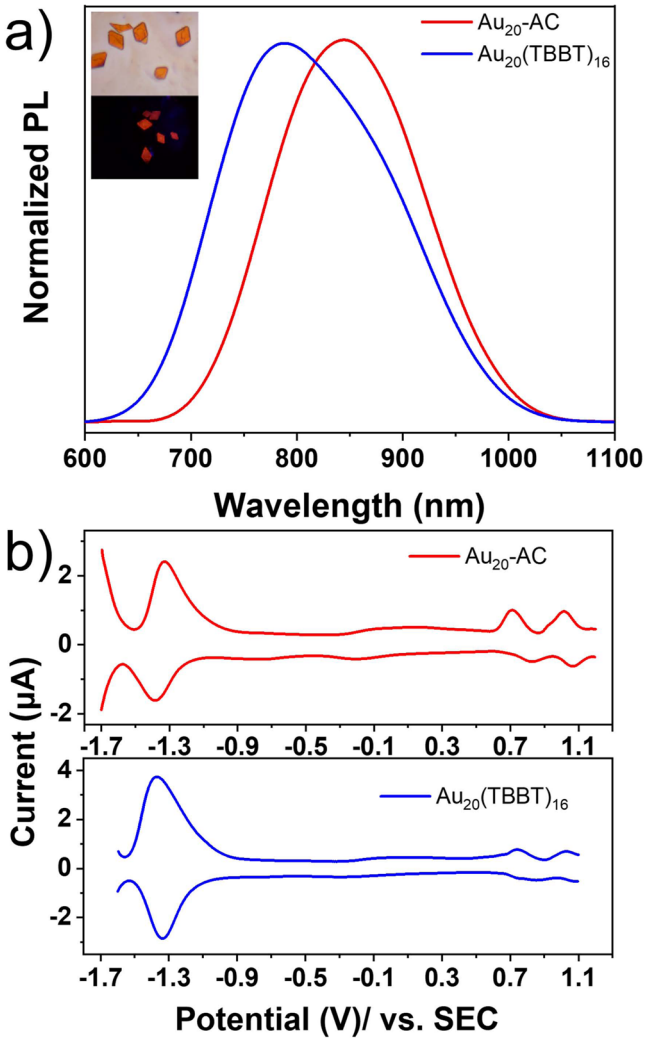

Fig. 2 Normalized PL of solid Au_{20}-AC and $Au_{20}(TBBT)_{16}$ and square wave voltammetry (SWV) of Au_{20}-AC and $Au_{20}(TBBT)_{16}$. a Normalized PL of solid Au_{20}-AC and $Au_{20}(TBBT)_{16}$. Inset: The crystal of Au_{20}-AC under visible light (top) and ultraviolet light (bottom), respectively. **b** SWV of 0.015 mM Au_{20}-AC and $Au_{20}(TBBT)_{16}$ in 1:1 TOL: ACN with 0.1 M TBAP. Pt disk was used as working electrode, Pt foil and SCE were used as counter and reference electrode, respectively.

Au_7 kernel comprised of two fused tetrahedra (Fig. 1a) arranged linearly through a common Au atom, different to the twisted tetrahedra found in $Au_{20}(TBBT)_{16}$. The average Au−Au bond length in the Au_7 kernel of Au_{20}-AC (2.730 Å) is slightly (0.40%) longer than that in $Au_{20}(TBBT)_{16}$ (2.719 Å). $Au_2(SR)_3$, $Au_3(SR)_4$ and circle-like $Au_6(SR)_6$ motifs were observed to cap the core tetrahedra (Fig. 1d, e, b). Interestingly, the mixed thiol ligands HSAdm and CHT comprise the $Au_3(SR)_4$ and $Au_6(SR)_6$ motifs, forming $Au_3(SAdm)_2(CHT)_2$ and $Au_6(SAdm)_4(CHT)_2$ motifs. The energy of Au_{20}-Iso1 was predicted to be comparable to or even lower than that of $Au_{20}(TBBT)_{16}$[34]. The use of mixed ligands instead of the more usual single thiol ligand might facilitate the experimental preparation of Au_{20}-Iso1. Regarding the Au_{20}-AC superstructure, the cyclohexane units present in the $Au_6(SAdm)_4(CHT)_2$ motifs adopt a chair configuration and are arranged in a head-to-head pattern due to the non-covalent interactions of C…H and H…H (Fig. 1g), contributing to the high stability of Au_{20}-AC in the aggregated state.

The composition of Au_{20}-AC was further confirmed by electrospray ionization mass spectrometry, X-ray photoelectron spectroscopy and thermogravimetric analysis. Cesium acetate (CsOAc) was added, to form adducts. As shown in Supplementary Fig. 3, the electrospray ionization mass spectra depicts a series of peaks, each separated by 52 Da and corresponding to a series of different Au_{20}-AC moieties. $[Au_{20}(C_{10}H_{15}S)_{16\text{-}n}(C_6H_{11}S)_n + Cs]^+$ $(n = 4\sim9)$ containing HSAdm and CHT ligands in different combinations, reflecting their dynamic equilibrium in the solution state. However, the crystal state Au_{20}-AC was determined by single crystal diffraction to contain 12 HSAdm and 4 CHT ligands. In mass spectrometry, the isotopic peaks of $[Au_{20}(SAdm)_{12}(CHT)_4 + Cs]^+$ are consistent with the simulated spectra (Supplementary Fig. 3). The composition of Au_{20}-AC was also confirmed by X-ray photoelectron spectrum (Supplementary Fig. 4) and thermogravimetric analysis (Supplementary Fig. 5).

Photoluminescence and voltammetry analysis of Au_{20} isomers. Au_{20}-AC and $Au_{20}(TBBT)_{16}$ in solid state were intensely photoluminescent. Figure 2a shows the PL spectra of solid Au_{20}-AC (red line) and $Au_{20}(TBBT)_{16}$ (blue line); the peaks are at 845 and 790 nm, respectively. A solution of Au_{20}-AC was non-fluorescent at the same excitation wavelength, reflecting its strong AIE behaviour (Supplementary Fig. 6). In the solution state, van der Waals forces drive the rotation of molecules until their surface motifs establish stable interactions with neighbouring nanoclusters; the free rotation of the ligands and any dissociation/association of the thiol ligands results in the loss of non-radiative energy[40]. Accordingly, Au_{20}-AC was barely luminescent in solution. However, the ligands of aggregated and crystallized nanoclusters are fixed. This restriction of intramolecular rotation (RIR) and suppression of any disaggregation and association processes inhibits the non-radiative decay of excited states, resulting in intense AIE in the solid state. The ligands of Au_{20}-AC are non-aromatic and thus unable to π–π stack, but their long-range interaction (between unit cells) may still affect their PL[40]. Aggregated Au_{20}-AC showed a longer PL lifetime (2.19 μs) than aggregated $Au_{20}(TBBT)_{16}$ (624 ns) (Supplementary Figs. 7 and 8).

Cyclic voltammetry (CV) studies of Au_{20}-AC and $Au_{20}(TBBT)_{16}$ were carried out by scanning between −1.7 and 1.2 V vs. SCE at a scan rate of 0.1 V s^{-1} (Supplementary Figs. 9 and S10). The square wave voltammetry (SWV) of Au_{20}-AC and $Au_{20}(TBBT)_{16}$ was tested in a 1:1 solution of toluene (TOL)/acetonitrile (ACN) with 0.1 M tetrabutylammonium perchlorate (TBAP) as the electrolyte. As shown in Fig. 2b, two quasi-reversible oxidation waves at $E_{Ox} = 0.71$ V and 1.01 V were observed (Fig. 2b, red line in top panel). These correspond to the Au_{20}-AC being oxidized consecutively to $[Au_{20}\text{-}AC]^{1+}$ and then $[Au_{20}\text{-}AC]^{2+}$. Au_{20}-AC shows one multi-electron reduction wave at $E_{Re} = -1.19$ V, which indicates an irreversible reduction process in Au_{20}-AC. Two oxidation peaks of $Au_{20}(TBBT)_{16}$ at 0.74 V and 1.02 V and a multi-electron reduction peak at −1.13 V were observed (Fig. 2b, blue line in down panel). All these redox processes of $Au_{20}(TBBT)_{16}$ are quasi-reversible. The potential differences between the first reduction and oxidation peak of Au_{20}-AC and $Au_{20}(TBBT)_{16}$ were 2.10 and 2.07 V. The surface ligands and motifs of Au_{20}-AC lowered its reduction and oxidation potentials compared to those of $Au_{20}(TBBT)_{16}$. The propensity of these nanoclusters to gain and lose electrons is related to their HOMO–LUMO gap and ligand-metal and metal-metal electronic coupling/interaction properties[41].

To rationalize the electrochemical properties of the gold clusters, DFT/PBE calculations were performed—the HOMO energies of Au_{20}-AC and $Au_{20}(TBBT)_{16}$ were calculated to be −4.23 eV and

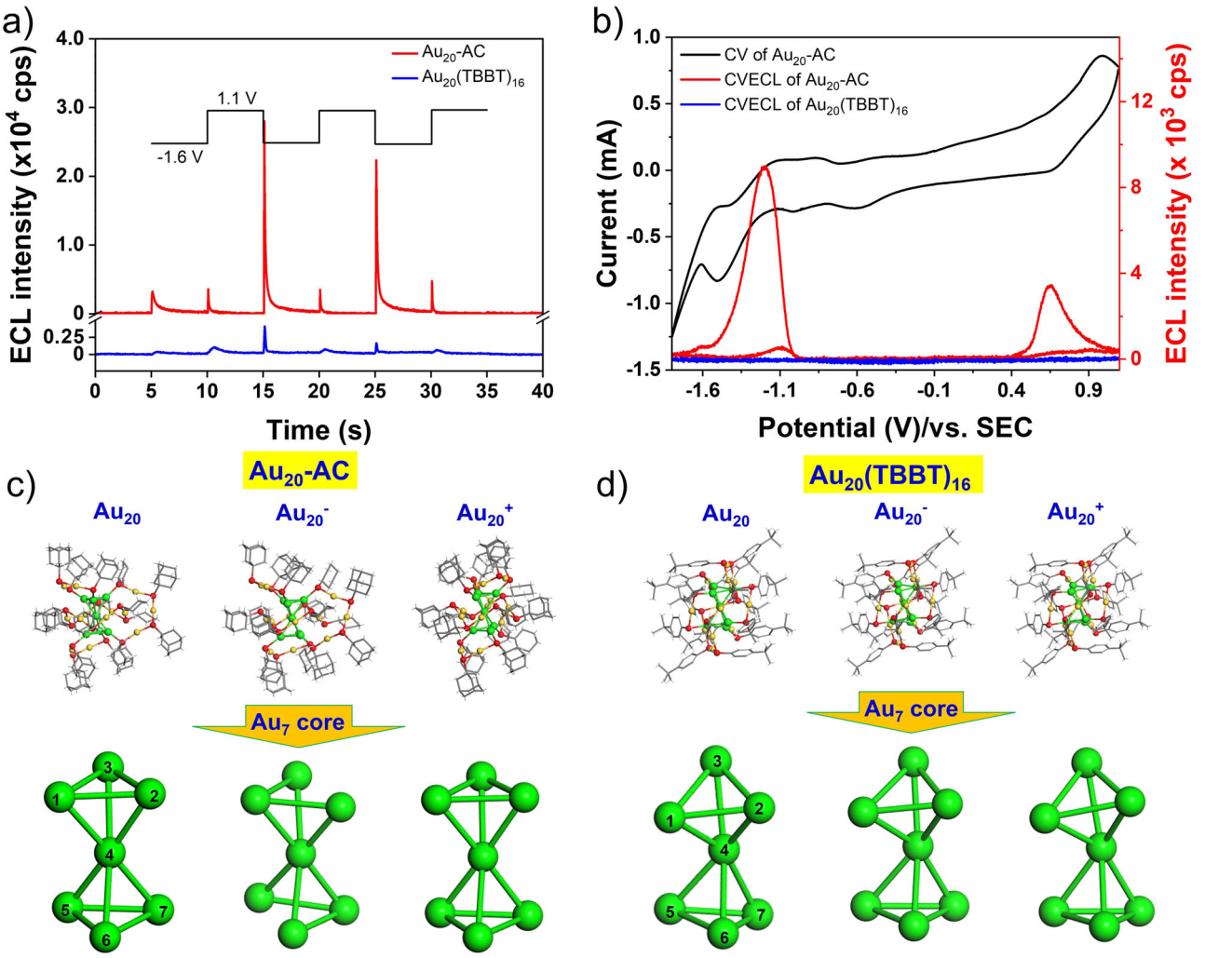

Fig. 3 ECL of Au_{20}-AC and $Au_{20}(TBBT)_{16}$ under potential step and scanning conditions and calculated stability of different valence states of Au_{20}-AC and $Au_{20}(TBBT)_{16}$ radical. a Potential step self-annihilation ECL of Au_{20}-AC and $Au_{20}(TBBT)_{16}$. The concentration of nanocluster is 0.015 mM in Tol/ACN (1:1) with 0.1 M TBAP electrolyte. The potential was set between −1.6 and 1.1 V and stepped cyclically, each potential was held for 5 s, and no potential was applied in the first and final 5 s. Pt mesh was used as working electrode, Pt foil and SCE were used as counter and reference electrode, respectively. **b** Self-annihilation ECL-voltage curves from −1.6 V to 1.1 V of Au_{20}-AC and $Au_{20}(TBBT)_{16}$ in solution state. Initial scan to negative potential direction. The 3rd cycle data was shown. **c**, **d** Theoretical calculation of structures of different valence states of Au_{20}-AC and $Au_{20}(TBBT)_{16}$ radical. The corresponding bond length is shown in Supplementary Table 2.

−4.41 eV, respectively (Supplementary Fig. 11). This is consistent with the lower oxidation potential of Au_{20}-AC compared to $Au_{20}(TBBT)_{16}$ (0.71 V vs 0.74 V); since the oxidation process involves removing an electron from the HOMO energy level, the Au_{20}-AC cluster with the higher HOMO energy level will lose an electron more easily compared to $Au_{20}(TBBT)_{16}$, whose lower HOMO energy level (−4.41 eV) is consistent with its higher relative oxidation potential (0.74 V). On the contrary, the LUMO energy level will acquire an electron during reduction, thus the Au_{20}-AC cluster with a higher LUMO energy level (−2.38 eV) will have more difficulty in obtaining an electron, resulting in a relatively low reduction potential (−1.19 V). The $Au_{20}(TBBT)_{16}$ cluster with a lower LUMO energy level (−2.74 eV) will have a relatively high reduction potential (−1.13 V). The HOMO-LUMO gaps of the Au_{20}-AC and $Au_{20}(TBBT)_{16}$ clusters are 1.85 eV and 1.67 eV, respectively. The DFT calculations are in good agreement with the experiments.

ECL of Au_{20} isomers in solution state and DFT theoretical analysis. The ECLs of both nanoclusters in solution state was studied in TOL/ACN (1:1) with Pt mesh and applied potential of between −1.6 V and 1.1 V. Figure 3a shows the step ECLs of both Au_{20} nanoclusters with negative and positive potentials alternately applied for three cycles. Overall, the ECL of Au_{20}-AC is stronger than that of $Au_{20}(TBBT)_{16}$. Au_{20}-AC shows intense ECL at −1.6 V (onset of 15 and 25 s) but weak ECL at 1.2 V (onset of 10, 20 and 30 s). In addition, the self-annihilation ECL of Au_{20}-AC and $Au_{20}(TBBT)_{16}$ were explored in potential scanning experiment. As shown in Fig. 3b, both cathodic and anodic ECL were observed in the 3rd cycle scanning potential for Au_{20}-AC and the onset potential of reductive ECL of Au_{20}-AC is at −1.0 V that is consistent with the onset potential of reduction peak in CV curve. No cathodic ECL signal was observed in the potential sweep of the first cycle because no cationic radicals were generated at this time (Supplementary Fig. 12). The ECL intensity of Au_{20}-AC under consecutive potential scans decreased slightly with relative standard deviation (RSD) of 7.52% (Supplementary Fig. 13). While $Au_{20}(TBBT)_{16}$ display quite weak self-annihilation ECL at all potentials (Fig. 3b, blue curve).

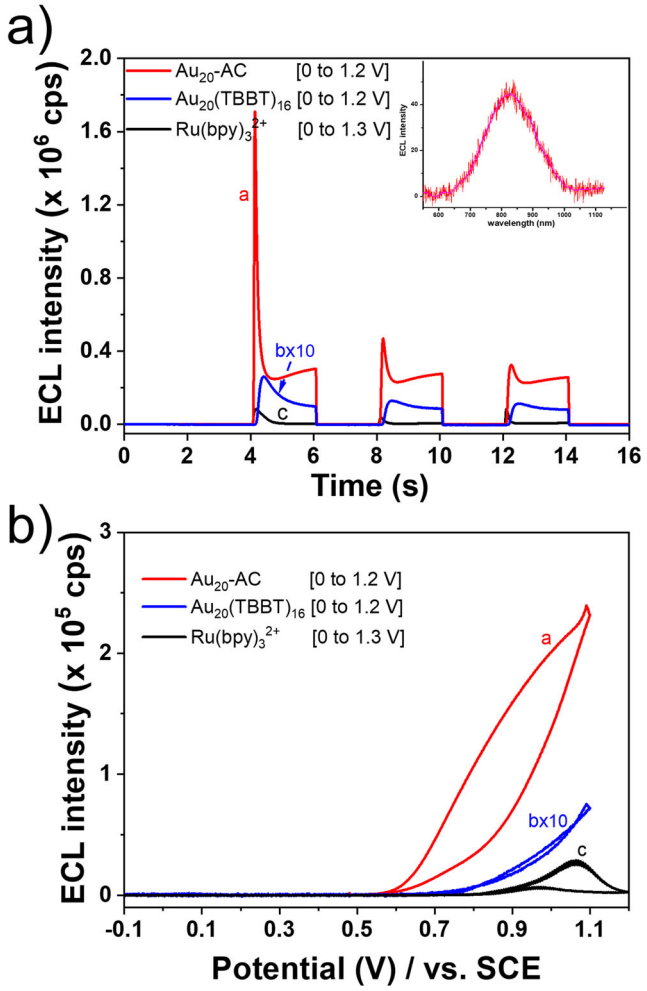

Fig. 4 Coreactant ECL of Au_{20}-AC, $Au_{20}(TBBT)_{16}$ and $Ru(bpy)_3^{2+}$ in solution state. Coreactant ECL of Au_{20}-AC, $Au_{20}(TBBT)_{16}$ and $Ru(bpy)_3^{2+}$ in solution state. Coreactant ECL experiments were executed in 1:1 TOL: ACN with 0.1 M TBAP and 5 mM TPrA. Pt mesh was used as working electrode, Pt foil and SCE were used as counter and reference electrodes, respectively. **a** Potential step coreactant ECLs of Au_{20}-AC, $Au_{20}(TBBT)_{16}$ and $Ru(bpy)_3^{2+}$ in solution state. Inset is the spectrum of Au_{20}-AC in solution state. The electrode potential was held for 2 s at denoted potentials in each step over three cycles. No potential was applied in the first and final 2 s. **b** ECL-voltage curves of Au_{20}-AC, $Au_{20}(TBBT)_{16}$ and $Ru(bpy)_3^{2+}$ in solution state. Potential scan rate is 0.1 V/s. The 3rd cycle data was shown.

To explore the influence factors of ECL performance of such two Au_{20} nanoclusters, we performed DFT calculations and studied the metal core and motif effects on their ECLs. As shown in Fig. 3c, d and Supplementary Table 2, both the Au2-Au3 and Au5-Au6 bond lengths in the Au_7 kernel of the $[Au_{20}\text{-AC}]^-$ anion were longer than those in the neutral Au_{20}-AC cluster (3.281 Å vs 2.810 Å and 3.050 Å vs 2.819 Å, respectively), reflecting their lower bond energies. There was no significant difference in the averaged Au-S distances in the core-shell and motif, indicating bare influence of different thiols and motifs on ECL performance (Supplementary Fig. 14 and Table 3). These bond length analyses and structural representations (Fig. 3c, d) indicate that the metal core of $[Au_{20}\text{-AC}]^-$ is distorted, reducing the overall stability of the $[Au_{20}\text{-AC}]^-$ and precluding its ability to react with cluster cations to form a strong anodic ECL signal (Fig. 3a, onset of 10, 20 and 30 s). The low stability of $[Au_{20}\text{-AC}]^-$ from theoretical simulations is consistent with the result obtained from voltammetric curves that $[Au_{20}\text{-AC}]^-$ is irreversible during the reduction process (Fig. 2b, top panel). However, more stable cluster radical cations can react with newly formed radical anions to form stronger cathodic ECL signals during the application of negative potential (Fig. 3a, onset of 15 and 25 s).

A possible self-annihilation ECL mechanism of the Au_{20} clusters is proposed in Supplementary Equation (1-4) (Supplementary Information Section 3); Au_{20} and Au_{20}* denote the ground- and excited-states of the Au_{20} (including Au_{20}-AC and $Au_{20}(TBBT)_{16}$) clusters, respectively. In the self-annihilation ECL process, negatively charged $Au_{20}^{-\cdot}$ and positively charged $Au_{20}^{+\cdot}$ cluster radicals are generated by electrode electron transfer reaction (Supplementary Equation (1) and (2)). Electrons or holes are transferred between cluster and the electrode surface. The generated radical cation and anion react and produce excited Au_{20}* (Supplementary Equation (3)), which relax to the ground state and release the energy via photon emission (Supplementary Equation (4)). The self-annihilation ECL intensity is dependent on the stabilities of the $Au_{20}^{-\cdot}$ and $Au_{20}^{+\cdot}$ intermediates that are generated on the electrode upon application of a potential. Simultaneously, the transfer rate of the electrons and holes, the reaction capability of radical anions and cations, and the radiative efficiency of the excited state will affect the ECL intensity. Although the metastability of anodic and cationic radicals of $Au_{20}(TBBT)_{16}$ cluster were not observed in the DFT theoretical simulation, its ECL signal was barely observed in potential and scanning experiments. Thus, we studied the emission capability of the excited states of Au_{20}-AC and $Au_{20}(TBBT)_{16}$. As shown in Supplementary Fig. 15 and Table 4, both excited nanoclusters displayed comparable emission capability. We speculate that the limited transfer rate of the electrons and holes and weak reaction capability between radical anions and cations may be responsible for the weak self-annihilation of $Au_{20}(TBBT)_{16}$.

ECL efficiency of Au_{20}-AC and $Au_{20}(TBBT)_{16}$ in solution state. The ECL efficiency of Au_{20}-AC and $Au_{20}(TBBT)_{16}$ is assessed by comparing to $Ru(bpy)_3^{2+}$-TPrA under the same measurement conditions. Figure 4a shows the step ECLs of Au_{20}-AC, $Au_{20}(TBBT)_{16}$ and $Ru(bpy)_3^{2+}$ in solution state in the prescnece of 5 mM TPrA as coreactant, in which "catalytic route" reactions occured[42]. The ECL efficiencies of Au_{20}-AC and $Au_{20}(TBBT)_{16}$ were evaluated by $Ru(bpy)_3^{2+}$/TPrA standard (Supplementary Fig. 16 and Table 5). The ECL efficiency of Au_{20}-AC/TPrA is more than 7 times higher than that of $Ru(bpy)_3^{2+}$/TPrA. Intense coreactant ECL of Au_{20}-AC allow its ECL spectrum to be collected. As shown the inset in Fig. 4a, Au_{20}-AC display an ECL emission band centered at 830 nm. In ECL-voltage curves, the ECL signal of Au_{20}-AC began to appear at about 0.5 V, and reached maximum at 1.1 V, while the signal of $Au_{20}(TBBT)_{16}$ is still very weak (Fig. 4b).

Solid-state ECL of Au_{20}-AC and $Au_{20}(TBBT)_{16}$ in coreaction pathway. Au_{20}-AC and $Au_{20}(TBBT)_{16}$ displayed red emission in solid state after light irradiation due to the AIE effect. With this in hand, we studied their SSECL. The SSECL of both nanoclusters was studied by separately loading 15 μg of each onto a GCE and allowing the electrode surface to dry in air. The electrochemical impedance spectroscopy (EIS) of both nanoclusters showed that their resistances are comparable (Supplementary Fig. 17), indicating a similar amount of both nanoclusters on electrode. The SSECL was conducted in 0.01 M phosphate buffer solution (PBS, pH = 7.5) in the presence of 0.1 M KCl as an electrolyte. As shown in Fig. 5, the similar oxidation potential of the cluster and coreactant is favorable to the ECL generation. Au_{20}-AC showed the strongest emission at 1.1 V (Fig. 5a),

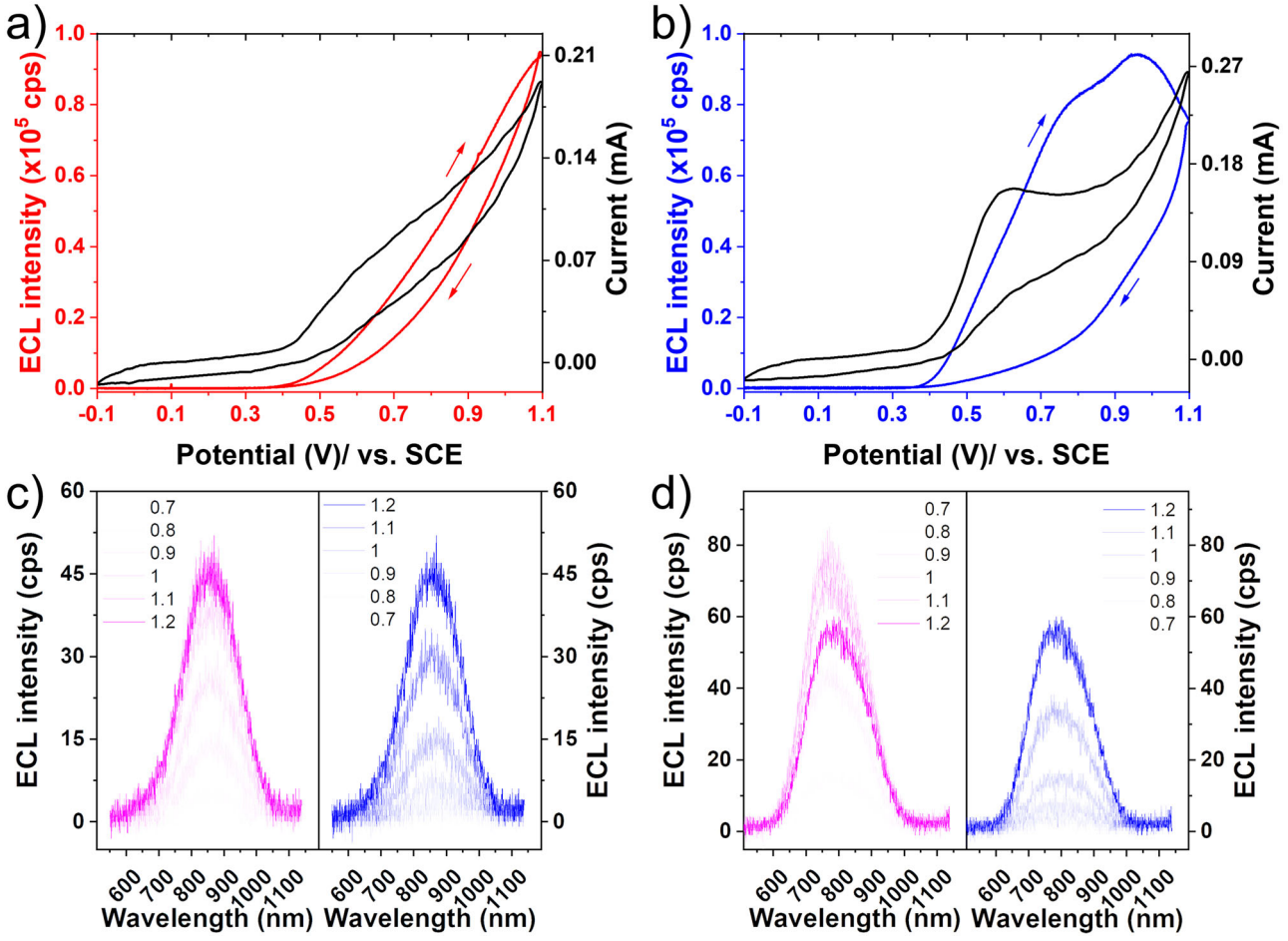

Fig. 5 Coreactant ECLs of Au_{20}-AC, $Au_{20}(TBBT)_{16}$ in solid state and their associated ECL spectra. a, **b** SSECL-voltage curves of Au_{20}-AC (red line) and $Au_{20}(TBBT)_{16}$ (blue line) in the presence of 5 mM TPrA. Coreactant SSECL experiments were carried out in 0.01 M PBS with 0.1 M KCl. 15 μg Au_{20}-AC and $Au_{20}(TBBT)_{16}$ were coated on GCE, Pt foil and SCE were used as counter and reference electrode. The potential was set from -0.1 to 1.1 V at 0.1 V/s. The 3rd cycle data was shown. **c**, **d** The SSECL spectra of Au_{20}-AC and $Au_{20}(TBBT)_{16}$ in the forward scan (pink) and reverse scan (blue). The potential was set from −0.1 to 1.1 V at 0.1 V/s with one spectrum collected every 1 s.

but $Au_{20}(TBBT)_{16}$ showed the strongest emission at 0.9 V in forward scan (Fig. 5b). The relatively strong SSECL of $Au_{20}(TBBT)_{16}$ may be due to the motif aggregation effect. The long eight-membered ring motif of $Au_{20}(TBBT)_{16}$ induces intense SSECL. The SSECLs of both Au_{20} nanoclusters are much higher than that of $Au_{25}(SC_2H_4Ph)_{18}$ whose sweeping potential ECL cannot be detected, and step ECL is quite weak (Supplementary Fig. 18). Both RIR and coreactant effects contribute significantly to the intense ECL performance. Intense SSECLs allow the spectra of Au_{20}-AC and $Au_{20}(TBBT)_{16}$ to be collected. The ECL spectra of Au_{20}-AC and $Au_{20}(TBBT)_{16}$ at various potentials are presented in Fig. 5c, d. No emission peak shift was observed for either Au_{20} cluster. All the peaks of Au_{20}-AC were centered at $\lambda_{max} = 860$ nm, and the strongest emission of $Au_{20}(TBBT)_{16}$ was at $\lambda_{max} = 770$ nm. Therefore, the ECL emission of Au_{20}-AC was 15 nm red-shifted compared to its PL emission, but the ECL emission of $Au_{20}(TBBT)_{16}$ was 20 nm blue-shifted compared to its PL emission. This slight difference between PL and ECL might reflect differences in their excited states[43].

Conclusions

The structurally predicted $Au_{20}(SAdm)_{12}(CHT)_4$ (Au_{20}-AC) nanocluster has been prepared and its electrochemiluminescence performance compared with that of its isomer $Au_{20}(TBBT)_{16}$. Au_{20}-AC showed a strongly cathodic and weakly anodic ECL via a self-annihilation pathway in solution state. By comparing the averaged Au-Au and Au-S distances in various gold cluster radicals, DFT simulation revealed the impact of the gold core on the electrochemiluminescence of Au_{20}-AC and its isomer $Au_{20}(TBBT)_{16}$. The $[Au_{20}\text{-AC}]^{\cdot-}$ with a deformed Au_7 kernel are metastable, which results in its weakly anodic ECL. Solid Au_{20}-AC and $Au_{20}(TBBT)_{16}$ both showed intense ECL in the presence of the TPrA co-reactant, and therefore are suitable for developing solid-state, anti-quenching ECL luminophores. Coreactant SSECL spectra were also collected, and their intense signals enabled ECL and PL to be compared. Further work to explore and address the interactions between the emitter, electrode, and solution interfaces are underway. This work provides insights into the relationship between the structure and ECL properties of atomic precision metal nanoclusters, and is expected to pave the way for new emitters that can be used for biosensing and immunoassays.

Materials and methods

Synthesis. Au_{20}-AC is prepared by ligand etching using $Au_{18}(CHT)_{14}$ as a precursor. $Au_{18}(CHT)_{14}$ nanoclusters were synthesized according to the method reported in the literature[39].

Step 1: Synthesis of $Au_{18}(CHT)_{14}$. 150 mg $HAuCl_4{\cdot}3H_2O$ and 260 mg L-glutathione were mixed with methanol for 15 min and then stirred at a lower speed. After 15 min, the mixture was diluted with a large amount (20 mL) of methanol, with high-speed stirring. After 15 min, a freshly prepared solution of sodium cyanoborohydride ($NaBH_3CN$, 63 mg in 5 ml methanol) was added. After 6 h, the methanol solution was dried and 20 mL H_2O and 20 mL dichloromethane (CH_2Cl_2) added. Excess cyclohexanethiol (1 mL) was added at 40 °C, to accomplish the two-

phase ligand exchange. After stirring for 10 hours, the dichloromethane phase was dried and the $Au_{18}(SC_6H_{11})_{14}$ residue thoroughly washed with methanol.

Step 2: Synthesis of $Au_{20}(SAdm)_{12}(CHT)_4$. 100 mg (598.80 μmol) 1-Adamantanethiol (HSAdm) was added to a solution of $Au_{18}(SC_6H_{11})_{14}$ (~10 mg, 1.94 μmol) in CH_2Cl_2 at 40 °C. After mixing overnight, the mixture was pipetted onto a TLC plate which was separated in a developing tank (CH_2Cl_2/Hex =1:4 v/v) (Supplementary Fig. 1). Bands corresponding to the different nanoclusters were removed and dissolved in CH_2Cl_2. Rhombic crystals of $Au_{20}(SAdm)_{12}(CHT)_4$ were obtained within 3 days via layer diffusion of methanol into a CH_2Cl_2 solution of the nanoclusters. The yield was about 10.2% based on the Au element (calculated from $HAuCl_4{\cdot}3H_2O$).

Electrochemical measurements. Electrochemical experiments were performed on a CHI 660e. A platinum mesh was used as the working electrode. A Pt foil and saturated calomel electrode (SCE) served as the counter and reference electrodes, respectively. The concentration of the samples was ~0.015 mM with 0.1 M TBAP in 10 ml toluene/acetonitrile (Volume ratio 1:1), and the solution was purged with argon for 15 min before experiments. All data were collected at room temperature.

ECL experiments were also performed with a three-electrode system in a quartz cuvette. A platinum mesh as the working electrode, which can provide a larger specific surface area compared to platinum disk electrodes. The dimensions of the platinum mesh electrodes used in the experiments are all 10 × 10 mm, and the effective surface area is 92.9 mm^2 according to the calculation formula $I = 2.69 \times 10^5 AD^{1/2}n^{3/2}v^{1/2}c$[44]. The cuvettes were aligned at a fixed position with respect to the camera for consistency. 15 μg samples were coated on glassy carbon electrode (GCE) for SSECL. A saturated calomel electrode (SCE) served as the reference electrode and a Pt foil as the counter electrode. The emission intensity was recorded with an Andor iDUS CCD camera (model No: DU401A-BR-DD). The camera was externally triggered by the potentiostat (Gamry Reference 600+) for synchronization. ECL spectra were collected with an Andor spectrograph (Kymera 193i). The sample solution was purged for about 15 min with argon prior to the measurements.

Data availability

The data that support the findings of this study, including supplementary method, figures, and tables, are available in its Supplementary Information files. Other relevant data are available from the corresponding author upon reasonable request. The X-ray crystallographic coordinates for structures of $Au_{20}(SAdm)_{12}(CHT)_4$ in this article can be found from Supplementary Data 1 or at the Cambridge Crystallographic Data Centre (CCDC: www.ccdc.cam.ac.uk) under accession number 2120320.

Received: 26 September 2022; Accepted: 19 May 2023;
Published online: 31 May 2023

References

1. Ding, Z. et al. Electrochemistry and electrogenerated chemiluminescence from silicon nanocrystal quantum dots. *Science* **296**, 1293–1297 (2002).
2. Li, L., Chen, Y. & Zhu, J. J. Recent advances in electrochemiluminescence analysis. *Anal. Chem.* **89**, 358–371 (2017).
3. Liu, Z., Qi, W. & Xu, G. Recent advances in electrochemiluminescence. *Chem. Soc. Rev.* **44**, 3117–3142 (2015).
4. Miao, W. Electrogenerated chemiluminescence and its biorelated applications. *Chem. Rev.* **108**, 2506–2553 (2008).
5. Zhang, Y. et al. Switching the photoluminescence and electrochemiluminescence of liposoluble porphyrin in aqueous phase by molecular. *Regul. Angew. Chem. Int. Ed.* **59**, 23261–23267 (2020).
6. Han, Z. et al. Electrochemiluminescence platforms based on small water-insoluble organic molecules for ultrasensitive aqueous-phase detection. *Angew. Chem. Int. Ed.* **58**, 5915–5919 (2019).
7. Tan, X., Zhang, B. & Zou, G. Z. Electrochemistry and electrochemiluminescence of organometal halide perovskite nanocrystals in aqueous medium. *J. Am. Chem. Soc.* **139**, 8772–8776 (2017).
8. Zhu, D. et al. Dual intrareticular oxidation of mixed-ligand metal-organic frameworks for stepwise electrochemiluminescence. *J. Am. Chem. Soc.* **143**, 3049–3053 (2021).
9. Murray, R. W. Nanoelectrochemistry: metal nanoparticles, nanoelectrodes, and nanopores. *Chem. Rev.* **108**, 2688–2720 (2008).
10. Carrara, S., Aliprandi, A., Hogan, C. F. & De Cola, L. Aggregation-induced electrochemiluminescence of platinum(II) complexes. *J. Am. Chem. Soc.* **139**, 14605–14610 (2017).
11. Wei, X. et al. Aggregation-induced electrochemiluminescence of carboranyl carbazoles in aqueous media. *Angew. Chem. Int. Ed.* **58**, 3162–3166 (2019).
12. Peng, H. et al. Dual enhancement of gold nanocluster electrochemiluminescence: electrocatalytic excitation and aggregation-induced emission. *Angew. Chem. Int. Ed.* **59**, 9982–9985 (2020).
13. Kwak, K. & Lee, D. Electrochemistry of atomically precise metal nanoclusters. *Acc. Chem. Res* **52**, 12–22 (2019).
14. Swanick, K. N., Hesari, M., Workentin, M. S. & Ding, Z. Interrogating near-infrared electrogenerated chemiluminescence of $Au_{25}(SC_2H_4Ph)_{18}^+$ clusters. *J. Am. Chem. Soc.* **134**, 15205–15208 (2012).
15. Hesari, M., Workentin, M. S. & Ding, Z. Highly efficient electrogenerated chemiluminescence of Au_{38} nanoclusters. *ACS Nano* **8**, 8543–8553 (2014).
16. Hesari, M. & Ding, Z. A grand avenue to Au nanocluster electrochemiluminescence. *Acc. Chem. Res* **50**, 218–230 (2017).
17. Tian, R. et al. Localization of Au nanoclusters on layered double hydroxides nanosheets: confinement-induced emission enhancement and temperature-responsive luminescence. *Adv. Funct. Mater.* **25**, 5006–5015 (2015).
18. Jin, R. C., Zeng, C. J., Zhou, M. & Chen, Y. X. Atomically precise colloidal metal nanoclusters and nanoparticles: fundamentals and opportunities. *Chem. Rev.* **116**, 10346–10413 (2016).
19. Liu, H. et al. Atomic-precision gold clusters for NIR-II imaging. *Adv. Mater.* **31**, e1901015 (2019).
20. Kang, X. & Zhu, M. Tailoring the photoluminescence of atomically precise nanoclusters. *Chem. Soc. Rev.* **48**, 2422–2457 (2019).
21. Hesari, M., Ding, Z. F. & Workentin, M. S. Electrogenerated chemiluminescence of monodisperse $Au_{144}(SC_2H_4Ph)_{60}$ clusters. *Organometallics* **33**, 4888–4892 (2014).
22. Chakraborty, I. & Pradeep, T. Atomically precise clusters of noble metals: emerging link between atoms and nanoparticles. *Chem. Rev.* **117**, 8208–8271 (2017).
23. Tian, S. et al. Structural isomerism in gold nanoparticles revealed by X-ray crystallography. [Corrected]. *Nat. Commun.* **6**, 8667 (2015).
24. Chen, Y. et al. Isomerism in $Au_{28}(SR)_{20}$ nanocluster and stable structures. *J. Am. Chem. Soc.* **138**, 1482–1485 (2016).
25. Xia, N. et al. Structural oscillation revealed in gold nanoparticles. *J. Am. Chem. Soc.* **142**, 12140–12145 (2020).
26. Qin, Z. et al. Atomically precise nanoclusters with reversible isomeric transformation for rotary nanomotors. *Nat. Commun.* **11**, 6019 (2020).
27. Hesari, M. & Ding, Z. Identifying highly photoelectrochemical active sites of two Au_{21} nanocluster isomers toward bright near-infrared electrochemiluminescence. *J. Am. Chem. Soc.* **143**, 19474–19485 (2021).
28. Mei, J., Leung, N. L. C., Kwok, R. T. K., Lam, J. W. Y. & Tang, B. Z. Aggregation-Induced Emission: Together We Shine, United We Soar! *Chem. Rev.* **115**, 11718–11940 (2015).
29. Luo, J. et al. Aggregation-induced emission of 1-methyl-1,2,3,4,5-pentaphenylsilole. *Chem. Commun.* **18**, 1740–1741 (2001).
30. Wei, X., Zhu, M. J., Yan, H., Lu, C. & Xu, J. J. Recent advances in aggregation-induced electrochemiluminescence. *Chemistry* **25**, 12671–12683 (2019).
31. Wong, J. M. et al. Revealing crystallization-induced blue-shift emission of a di-boron complex by enhanced photoluminescence and electrochemiluminescence. *Angew. Chem. Int. Ed.* **59**, 17461–17466 (2020).
32. Wu, Z. et al. Unraveling the impact of gold(I)-thiolate motifs on the aggregation-induced emission of gold nanoclusters. *Angew. Chem. Int. Ed.* **59**, 9934–9939 (2020).
33. Luo, Z. T. et al. From aggregation-induced emission of Au(I)-thiolate complexes to ultrabright Au(0)@Au(I)-thiolate core-shell nanoclusters. *J. Am. Chem. Soc.* **134**, 16662–16670 (2012).
34. Wang, P. et al. A revisit to the structure of $Au_{20}(SCH_2CH_2Ph)_{16}$: a cubic nanocrystal-like gold kernel. *Nanoscale* **10**, 10357–10364 (2018).
35. Zeng, C., Liu, C., Chen, Y., Rosi, N. L. & Jin, R. Gold-thiolate ring as a protecting motif in the $Au_{20}(SR)_{16}$ nanocluster and implications. *J. Am. Chem. Soc.* **136**, 11922–11925 (2014).
36. Liao, Y. H. et al. In-situ produced ascorbic acid as coreactant for an ultrasensitive solid-state tris(2,2 ‘-bipyridyl) ruthenium(II) electrochemiluminescence aptasensor. *Biosens. Bioelectron.* **26**, 4815–4818 (2011).
37. Jin, Z. C. et al. Electroactive metal-organic frameworks as emitters for self-enhanced electrochemiluminescence in aqueous medium. *Angew. Chem. Int. Ed.* **59**, 10446–10450 (2020).
38. Zhang, H. et al. Bacteria photosensitized by intracellular gold nanoclusters for solar fuel production. *Nat. Nanotechnol.* **13**, 900 (2018).
39. Chen, S. et al. The structure and optical properties of the $[Au_{18}(SR)_{14}]$ nanocluster. *Angew. Chem. Int. Ed.* **54**, 3145–3149 (2015).
40. Li, Y. et al. Double-helical assembly of heterodimeric nanoclusters into supercrystals. *Nature* **594**, 380–384 (2021).
41. Lee, D., Donkers, R. L., DeSimone, J. M. & Murray, R. W. Voltammetry and electron-transfer dynamics in a molecular melt of a 1.2 nm metal quantum dot. *J. Am. Chem. Soc.* **125**, 1182–1183 (2003).
42. Miao, W., Choi, J.-P. & Bard, A. J. Electrogenerated Chemiluminescence 69: The Tris(2,2‘-bipyridine)ruthenium(II), $(Ru(bpy)_3^{2+})$/Tri-n-propylamine (TPrA) System RevisitedA New Route Involving $TPrA^{\bullet+}$ Cation Radicals. *J. Am. Chem. Soc.* **124**, 14478–14485 (2002).
43. Chen, S. et al. Near infrared electrochemiluminescence of rod-shape 25-atom AuAg nanoclusters that is hundreds-fold stronger than that of $Ru(bpy)_3$ standard. *J. Am. Chem. Soc.* **141**, 9603–9609 (2019).

44. Song, X. et al. Peptide-based electrochemiluminescence biosensors using silver nanoclusters as signal probes and Pd-Cu_2O hybrid nanoconcaves as coreactant promoters for immunoassays. *Anal. Chem.* **93**, 13045–13053 (2021).

Acknowledgements

We acknowledge the finical support of the NSFC (Grant Nos. 21631001, 22004001), the Ministry of Education, the Ministry of Education and Education Department of Anhui Province (2008085QB84), and the University Synergy Innovation Program of Anhui Province (GXXT-2020-053). Y.P. acknowledges financial support from the NSFC (91961121).

Author contributions

S.C., Y.L., and K.K. synthesized the samples and carried out the experimental tests. B.Y., X.W., and L.J., synthesized the samples. P.W. and Y.P. performed the DFT calculations. S.C. and Y.L. solved the crystal structures. S.C., P.W., Y.P., and M.Z. designed the study. S.C., Y.L., and P.W. wrote the manuscript. All authors discussed the results and commented on the manuscript.

Competing interests

The authors declare no competing interests.

Additional information

Supplementary information The online version contains supplementary material available at https://doi.org/10.1038/s42004-023-00907-4.

Correspondence and requests for materials should be addressed to Shuang Chen, Pu Wang, Yong Pei or Manzhou Zhu.

Peer review information *Communications Chemistry* thanks Zhifeng Ding, Jun-Jie Zhu and the other, anonymous, reviewer(s) for their contribution to the peer review of this work.